

Shocked Molecular Hydrogen in the 3C 326 Radio Galaxy System

Patrick Ogle¹, Robert Antonucci², P. N. Appleton³, & David Whysong⁴

¹*Spitzer Science Center, California Institute of Technology, Mail Code 220-6, Pasadena, CA 91125*

²*Physics Dept., University of California, Santa Barbara, CA 93106*

³*NASA Herschel Science Center, California Institute of Technology, Mail Code 100-22, Pasadena, CA 91125*

⁴ *NRAO, Array Operations Center, P. O. Box 0, 1003 Lopezville Rd., Socorro, NM 87801-0387*

ogle@ipac.caltech.edu

ABSTRACT

The *Spitzer* spectrum of the giant FR II radio galaxy 3C 326 is dominated by very strong molecular hydrogen emission lines on a faint IR continuum. The H₂ emission originates in the northern component of a double-galaxy system associated with 3C 326. The integrated luminosity in H₂ pure-rotational lines is 8.0×10^{41} erg s⁻¹, which corresponds to 17% of the 8-70 μ m luminosity of the galaxy. A wide range of temperatures (125-1000 K) is measured from the H₂ 0-0 S(0)-S(7) transitions, leading to a *warm* H₂ mass of $1.1 \times 10^9 M_{\odot}$. Low-excitation ionic forbidden emission lines are consistent with an optical LINER classification for the active nucleus, which is *not* luminous enough to power the observed H₂ emission. The H₂ could be shock-heated by the radio jets, but there is no direct indication of this. More likely, the H₂ is shock-heated in a tidal accretion flow induced by interaction with the southern companion galaxy. The latter scenario is supported by an irregular morphology, tidal bridge, and possible tidal tail imaged with IRAC at 3-9 μ m. Unlike ULIRGs, which in some cases exhibit H₂ line luminosities of comparable strength, 3C 326 shows little star-formation activity ($\sim 0.1 M_{\odot}$ yr⁻¹). This may represent an important stage in galaxy evolution. Starburst activity and efficient accretion onto the central supermassive black hole may be delayed until the shock-heated H₂ can kinematically settle and cool.

Subject headings: galaxies: active, galaxies: jets, infrared: galaxies

1. Introduction

Recent *Spitzer* and ISO observations have revealed a new class of extremely luminous molecular hydrogen emission galaxies (MOHEG’s) with $L(\text{H}_2) = 10^{40} - 10^{43} \text{ erg s}^{-1}$ in pure-rotational molecular hydrogen emission lines but relatively weak total IR emission, $L(\text{H}_2)/L(\text{IR}) > 10^{-3}$. In comparison, normal star-forming galaxies in the SINGS survey of the local universe have $L(\text{H}_2)/L(\text{IR}) \sim 6 \times 10^{-4}$ (Roussel et al. 2007).

Appleton et al. (2006) discovered H_2 emission extended over $50''$ in the giant intergalactic X-ray shock front in the Stephan’s Quintet compact group. The estimated H_2 luminosity from the whole shock is in excess of 10^{41} ergs/s . Nearly 30% of the IR luminosity is in H_2 lines, while the rest is emitted by $\sim 40 \text{ K}$ dust in the far-IR (Xu et al. 2003). The power in the H_2 lines compared with the dust continuum is several orders of magnitude larger than that seen in photo-dissociation regions (PDRs). The H_2 emission lines are very broad (870 km s^{-1}), suggesting turbulent motions inside the shock front. The H_2 emission may be powered by non-dissociative shocks in dense clumps or filaments inside the shock front.

Egami et al. (2006) find extremely luminous $L(\text{H}_2) = 2 \times 10^{43} \text{ erg s}^{-1}$ emission from $\sim 10^{10} M_\odot$ of warm H_2 in the brightest galaxy of the high-luminosity X-ray cluster Zw 3146. This is accompanied by high-luminosity dust emission powered by starburst activity. Lower luminosity ro-vibrational H_2 emission is similarly seen in several low-redshift galaxy clusters (Donahue et al. 2000; Hatch et al. 2005; Johnstone et al. 2007). The source of excited H_2 in galaxy clusters is an unsolved mystery—cooling flows, jet shocks, and X-ray heating by active galactic nuclei (AGNs) have all been considered.

Molecular hydrogen emission is often seen in interacting galaxies and ultra-luminous infrared galaxies (ULIRGs), but $L(\text{H}_2)/L(\text{IR})$ is typically $\ll 10^{-3}$ (Haas et al. 2005; Higdon et al. 2006). The late-stage merger/LIRG NGC 6240 has atypically luminous emission from $1.6 \times 10^9 M_\odot$ of warm H_2 , accompanied by a prodigious star-formation rate of $\sim 120 M_\odot \text{ yr}^{-1}$ (Lutz et al. 2003; Netzer et al. 2005; Max et al. 2005; Armus et al. 2006). The overlap region between the Antennae colliding galaxies also shows unusually strong H_2 emission with $L(\text{H}_2)/L(\text{IR}) \sim 1 \times 10^{-3}$, possibly indicating a pre-starburst shock (Haas et al. 2005).

We present the remarkable H_2 emission spectrum of the FR II radio galaxy 3C 326, observed with the *Spitzer* Space Telescope. This is part of a large survey of 52 FR II radio galaxies from the 3CRR catalog (Ogle, Whysong, & Antonucci 2006), and another survey of 21 FR I radio galaxies (Ogle, Antonucci, & Whysong 2007). So far, we have found 3 FR IIs (6%) and 5 FR Is (24%) with strong H_2 emission (Ogle et al. 2007, in preparation). Of the galaxies in our sample, 3C 326 has the largest H_2 emission line equivalent widths. The

weak mid-IR continuum of 3C 326 indicates the presence of a radiatively inefficient AGN, in spite of its large radio power and enormous size of its radio lobes.

2. Radio Galaxy Identification

The radio source 3C 326 is one of the largest known (Willis & Strom 1978), with an angular size of $19''.5$ (1.9 Mpc; we assume a cosmology with $H_0 = 70 \text{ km s}^{-1} \text{ Mpc}^{-1}$, $\Omega_m = 0.3$, and $\Omega_\Lambda = 0.7$). The pair of galaxies 3C 326 N and 3C 326 S are both at a redshift of $z = 0.089 \pm 0.001$ and have a projected separation of $24''.9$ (41 kpc). There is some confusion concerning which of the two galaxies hosts the AGN that produced the Mpc-scale radio lobes. *Both* galaxies have unresolved ($< 3''$) radio sources coincident with their nuclei, with $S_\nu(8 \text{ GHz}) = 1.5$ and 6.5 mJy , respectively (Rawlings et al. 1990). While the southern radio source is brighter, both sources are consistent with typical FR II radio galaxy cores. The galaxy 3C 326 N has a LINER-like optical emission line spectrum (strong [OII], H α , [S II], and weak [OIII]), while 3C 326 S has no detected emission lines (Rawlings et al. 1990; Simpson et al. 1996). Also, the K-band magnitude and corresponding stellar mass of 3C 326 N is more typical of FR II radio galaxy hosts (Rawlings et al. 1990). We therefore targeted 3C 326 N with the *Spitzer* IRS.

3. Observations

3.1. Spitzer IRS

The radio galaxy 3C 326 N was observed with the *Spitzer* IRS (Houck et al. 2004), covering the wavelength range $5\text{--}35 \mu\text{m}$. The companion galaxy 3C 326 S was observed on one nod of the Short-Low (SL) slits because of a fortuitous slit PA (Fig.1). The slit widths in the low-resolution modules Short-Low 2 (SL2), Short-Low 1 (SL1), Long-Low 2 (LL2), and Long-Low 1 (LL1) are $3''.6$, $3''.7$, $10''.5$, and $10''.7$, respectively. The SL and LL spectral resolutions range from 60-130. The exposure times were 240 seconds in each spectral order except LL2 (480 seconds).

Our data reductions began from the S15.3.0 pipeline-processed basic calibrated data (BCDs). Off-slit observations were subtracted to remove background light. The 2D-spectra were cleaned using IRSCLEAN 1.8 to median filter bad pixels. Spectra were extracted using SPICE 1.4 within tapered regions matching the *Spitzer* point-spread function (SL2: $7''.2$ at $6 \mu\text{m}$, SL1: $14''.4$ at $12 \mu\text{m}$, LL2: $21''.7$ at $16 \mu\text{m}$, LL1: $36''.6$ at $27 \mu\text{m}$). The second LL2 nod was considerably noisier than the first, so we discarded this data. Optimal extraction (which

assumes a point-source spatial profile) yielded significant gains in S/N for both galaxies.

At the redshift of 3C 326, $1''0$ corresponds to 1.7 kpc. The SL and LL slit widths correspond to 6.2 kpc and 18 kpc, respectively, and are considerably smaller than the optical extents of the two galaxies. However, the continuum level is well-matched across orders and the emission lines and dust features do not appear to be spatially extended along the slit for either galaxy (Figs. 1, 2, 3). The continuum and emission line fluxes from the optimally extracted spectra also agree well with the regular extractions, indicating that the galaxies are (excepting the stellar component at short wavelengths) mostly unresolved by *Spitzer* IRS, and that aperture effects are unimportant for studying the dust and gas emission.

3.2. The Mid-IR Spectra

The spectrum of 3C 326 N is dominated by pure-rotational emission lines from molecular hydrogen (Fig. 2, Table 1). We detect the full series of emission lines from H_2 0-0 S(0)-S(7). Forbidden emission lines from the low-moderate ionization species Fe II, S IV, Ne II, S III, and O IV are also observed (Table 2). Polycyclic aromatic hydrocarbon (PAH) emission features are seen at 6.7, 7.7, 10.7, 11.3, 13.6, and 17 μm (Table 3). We consider the PAHs at 6.7, 7.7, 10.7, 15.9 and 18.9 μm and the Fe II, S IV, and S III lines to be marginal ($< 3\sigma$) detections.

We model the 3C 326 N spectrum using the χ^2 fitting routine PAHFIT (Smith et al. 2007). Extinction is not included in the model since it does not improve the fit. Emission lines are fit by Gaussians and PAH features are fit by Drude profiles (Tables 1-3). None of the emission lines are resolved, all with $\text{FWHM} < 2300 - 5000 \text{ km s}^{-1}$. The 4.8-8 μm continuum is dominated by galaxian starlight. An excess over the stellar component in the 8-24 μm region is fit by thermal emission from warm (90-300 K) dust, with integrated flux $F_{8-24} = 9.0 \pm 0.9 \times 10^{-14} \text{ erg s}^{-1} \text{ cm}^{-2}$ and luminosity $L_{8-24} = 1.8 \pm 0.2 \times 10^{42} \text{ erg s}^{-1}$.

The companion galaxy 3C 326 S has no H_2 emission detected; the 3σ upper limit to the H_2 S(3) line flux is $1.2 \times 10^{-15} \text{ erg s}^{-1} \text{ cm}^{-2}$ ($L(H_2) < 2.4 \times 10^{40} \text{ erg s}^{-1}$). No ionic forbidden emission lines are detected, consistent with the lack of optical emission lines and indicating an inactive nucleus. A spike in the spectrum at $\sim 12 \mu\text{m}$ does not match any known emission lines and may result from a hot pixel. The 7.7 and 11.3 PAH features are 2-3 times as strong in 3C 326 S compared to 3C 326 N (Table 3) and the mean 9-10 μm continuum flux density ($0.62 \pm 0.04 \text{ mJy}$) is 20% brighter.

3.3. Spitzer IRAC and MIPS

We retrieved the IRAC (Fazio et al. 2004) 3.6, 4.5, 5.8, and 8.0 μm S14.0.0-processed images from the *Spitzer* archive (Program-ID 03418, PI M. Birkinshaw) to further constrain the spatial distribution of the stellar, dust, and molecular gas components (Figs. 3,4). A 3σ clipped average of the dither positions, excluding frames affected by a bright star at the edge of the field, was used to subtract the background light, and frames were combined using the SSC MOPEX-MOSAIC software. The 3.6 and 4.5 μm bands measure the stellar continuum. The 5.8 μm band contains the redshifted H_2 S(5)-S(7) lines and 6.7 μm PAH feature. The 8.0 μm band contains the redshifted H_2 S(3)-S(4) lines and 7.7 μm PAH feature. Both of the latter two bands also contain thermal continuum emission from warm dust.

The irregular morphology of 3C 326 N in the IRAC images suggests an ongoing interaction or merger with 3C 326 S (24''9 at PA= 177°), a relatively compact elliptical galaxy. The isophotes of the two galaxies merge and they appear to be connected by a tidal bridge. There is a possible tidal tail extending from the NW quadrant at PA= 290 – 334°. Two other sources, one 4''3 away from the center of 3C 326 at PA= 111° and one 15''9 away at PA= 268°, appear to be unrelated background galaxies seen in projection, based on their morphologies, red colors, and small angular diameters in archival Sloan Digital Sky Survey (SDSS) images ¹.

We also obtained 24, 70, and 160 μm MIPS (Rieke et al. 2004) imaging data from the Spitzer archive for 3C 326 (Fig. 5). Individual BCD frames from the S14.4 pipeline were processed with the MOPEX-MOSAIC software to generate final images. Aperture photometry was performed on both 3C 326 N and 3C 326 S, and point-source aperture corrections² were applied to derive the fluxes (Table 4 and Fig. 6). Both galaxies are detected at 24 and 70, but not 160 μm . We measure a root-mean-square noise of 0.4 MJy sr^{-1} and 3σ flux upper limits of 34 mJy at 160 μm . This is consistent with a non-detection at 870 μm (Quillen et al. 2003), within a 23'' beam centered on 3C 326 S.

The companion 3C 326 S is twice as bright as 3C 326 N at 24 μm , while 3C 326 N is 40% brighter at 70 μm . A third source is seen in the 70 μm image at the location where the tidal bridge in the IRAC 3.6 μm image connects to 3C 326 N (Fig.5, Table 4). It is not detected in the MIPS 24 μm band, nor in any of the IRAC bands. If it is truly associated with 3C 326, then it may indicate cool dust in the tidal bridge. Unfortunately, none of the IRS slits covered this feature, so we do not know if there is any associated H_2 emission.

¹<http://www.sdss.org/>

²obtained from <http://ssc.spitzer.caltech.edu>

The spectral energy distributions (SEDs) of 3C 326 N and S are similar, but do show interesting differences (Fig. 6). Both are dominated by stellar emission at frequencies $> 4 \times 10^{13}$ Hz (wavelengths $< 8 \mu\text{m}$), consistent with our model of the IRS spectrum of 3C 326 N. Dust emission contributes most of the flux at $\sim 1 \times 10^{12} - 4 \times 10^{13}$ Hz and synchrotron emission from the radio cores is seen at 3-10 GHz. The ratio $L(70 \mu\text{m})/L(24 \mu\text{m})$ is greater in 3C 326 N than in 3C 326 S (Table 4), indicating relatively more cool dust emission and relatively less warm dust emission.

We estimate far-IR continuum luminosities by interpolating the 24 and 70 μm photometric points with a power law. This yields $L_{24-70} = 3.0 \pm 0.4 \times 10^{42}$ erg s $^{-1}$ and $3.3 \pm 1.8 \times 10^{42}$ erg s $^{-1}$, respectively, for 3C 326 N and 3C 326 S. Adding together the MIR 8-24 μm and FIR 24-70 μm emission, the 8-70 μm luminosity of 3C 326 N is $L_{8-70} = 4.8 \pm 0.5 \times 10^{42}$ erg s $^{-1}$ ($1.2 \pm 0.1 \times 10^9 L_{\odot}$). Upper and lower bounds to the FIR luminosity at longer wavelengths of $L_{70-1000} = 0.3 - 1.7 \times 10^{43}$ erg s $^{-1}$ are estimated for either galaxy by assuming blackbody emission that peaks at either 70 μm or 160 μm (Fig. 6). The total 8-1000 μm IR luminosity of 3C 326 N therefore lies in the range $L_{\text{IR}} = 0.8 - 2.2 \times 10^{43}$ erg s $^{-1}$ ($2 - 6 \times 10^9 L_{\odot}$).

4. H₂ Emission

The galaxy 3C 326 N has H₂ pure-rotational lines of extraordinary luminosity and equivalent width (Fig. 2, Table 1). The H₂ S(3) line has a luminosity of $2.34 \pm 0.08 \times 10^{41}$ erg s $^{-1}$ and an equivalent width of $0.80 \pm 0.08 \mu\text{m}$. The integrated S(0)-S(7) line luminosity is $L(\text{H}_2) = 8.0 \pm 0.4 \times 10^{41}$ erg s $^{-1}$. This is $17 \pm 2\%$ of the measured 8-70 μm luminosity and 4 – 10% of the estimated 8-1000 μm luminosity, making it the most extreme H₂-emitting galaxy seen so far by Spitzer (Table 6). Unlike the giant, extended, intergalactic shock in Stephan’s Quintet, the H₂ emission here is unresolved and contained within the central region of 3C 326 N.

We estimate the upper-level column densities (N/g) for each observed H₂ transition, divided by the statistical weights (Fig. 7, Table 1), assuming that the H₂ source just fits inside the SL slit (3''.7). The column density distribution is fit by a minimum of 3 temperature components with $T = 125, 400$, and 1000 K (Table 5). The fit is not unique but rather serves to demonstrate the large range of temperatures of the H₂ emission regions. The total column density of 125 K H₂ averaged over the SL slit is 1.8×10^{21} cm $^{-2}$.

The ratio of ortho (odd angular momentum quantum number J) to para (even J) H₂ depends on the gas temperature and thermal history. Warm H₂ in thermal equilibrium at a temperature of 125 K should have ortho/para=2.1, which is consistent with our model fit.

The ratio of ortho/para H_2 in the hot (400 K and 1000 K) components is consistent with the standard value of 3.0 for gas in thermal equilibrium at $T > 250$ K (Wilgenbus et al. 2000; Neufeld et al. 2006).

The masses of *warm* and *hot* molecular gas sum to $1.1 \times 10^9 M_\odot$ (Table 6). This is comparable to the warm H_2 mass in NGC 6240 (Lutz et al. 2003; Armus et al. 2006) and to the *total* molecular gas mass of the Milky Way ($\sim 2 \times 10^9 M_\odot$). No published CO observations of 3C 326 are available, so we have no knowledge of the mass of cold H_2 ; although by analogy with galaxies like NGC 6240 the cold component could be even larger than the warm and hot components. In thermodynamic equilibrium, the H_2 component densities must exceed the critical densities of the observed rotational transitions (Le Boulton et al. 1999). This yields maximum filling factors ranging from $f_{\text{max}} = 2 \times 10^{-3}$ for the 125 K component to $f_{\text{max}} = 1 \times 10^{-9}$ for the 1000 K component within the central 6.2 kpc-diameter sphere (Table 5).

5. Forbidden Emission Lines and AGN Activity

The mid-IR forbidden emission lines from several ions (Table 2) can be used to distinguish between starburst and AGN activity. In particular, line flux ratios of $[\text{O IV}]/[\text{Ne II}] = 0.6 \pm 0.1$ and $[\text{S IV}]/[\text{Ne II}] = 0.08 \pm 0.04$ in 3C 326 are characteristic of a LINER AGN (Spinoglio & Malkan 1992; Sturm et al. 2006). Seyfert galaxies have relatively stronger $[\text{O IV}]$ and $[\text{S IV}]$ than this, while starburst galaxies are relatively weaker in these two lines. Consequently, little of the forbidden line emission comes from star-formation activity. A LINER classification for 3C 326 is also consistent with the optical line ratio $[\text{O III}] 5007\text{\AA}/[\text{O II}] 3727\text{\AA} = 0.30$ (Simpson et al. 1996).

Spitzer observations give an *upper limit* to the IR luminosity of the AGN, since there is a significant contribution from the host galaxy. The fiducial $15 \mu\text{m}$ continuum flux is 0.87 ± 0.09 mJy, somewhat greater than the upper limit measured by Ogle, Whysong, & Antonucci (2006). (Our measurement accuracy has improved by throwing out the noisy LL2 nod and using optimal extraction.) The corresponding luminosity is $\nu L(15 \mu\text{m}) = 3.4 \pm 0.4 \times 10^{42}$ erg s^{-1} and its ratio to the radio lobe luminosity is only $\nu L(15 \mu\text{m})/\nu L(178 \text{ MHz}) = 4.4$. We confirm that this powerful radio galaxy contains an AGN with relatively low accretion power. In comparison, we find from archival *Spitzer* IRS observations that the LINER/FR I radio galaxy M 87 is one tenth as bright, with $\nu L(15 \mu\text{m}) = 3.3 \pm 0.1 \times 10^{41}$ erg s^{-1} , and has a similar ratio of $\nu L(15 \mu\text{m})/\nu L(178 \text{ MHz}) = 3.9$. It has been argued that low-power radio galaxies such as M 87 are fueled by radiatively inefficient accretion (Reynolds et al. 1996).

X-ray heating has been proposed as a possible mechanism to produce H_2 emission in active galaxies (Krolik & Lepp 1989; Draine & Woods 1990; Rigopoulou et al. 2002). Unfortunately, there are no published X-ray observations of 3C 326 N. However, Hardcastle, Evans, & Croston (2006) find a $\sim 1:1$ correlation between $15\ \mu\text{m}$ continuum emission and accretion-powered 2–10 keV X-ray luminosity for $z < 0.5$ radio galaxies. If this correlation holds true for 3C 326 N and the H_2 were powered by X-rays, then the observed ratio of $L(\text{H}_2)/L(15\ \mu\text{m}) = 0.23 \pm 0.03$ would require an implausibly high conversion of X-rays to H_2 emission. *Chandra* X-ray observations are necessary to directly confirm this, and will also be useful for measuring the high-energy SED of the AGN to test accretion models.

6. Aromatic Feature Emission and Star Formation

We detect several aromatic (PAH) emission features in the IRS spectrum of 3C 326 N (Fig.2, Table 3). The 7.7 and $11.3\ \mu\text{m}$ PAH luminosities are $1.0 \pm 0.5 \times 10^{41}\ \text{erg s}^{-1}$ and $1.3 \pm 0.3 \times 10^{41}\ \text{erg s}^{-1}$, respectively. The $11.3/7.7$ PAH flux ratio is 1.2 ± 0.6 , to be compared with an average ratio of 0.3 ± 0.1 for spiral galaxies and AGN host galaxies (Smith et al. 2007; Shi et al. 2007). The total luminosity in detected PAH features is $L(\text{PAH}) = 1.0 \pm 0.1 \times 10^{42}\ \text{erg s}^{-1}$ and the ratio $L(\text{H}_2)/L(\text{PAH}) = 0.8 \pm 0.1$. This ratio is much greater than the typical ratio of $\sim 1 \times 10^{-2}$ seen in normal star-forming galaxies where both H_2 and PAHs are thought to be produced in stellar PDRs (Roussel et al. 2007).

PAH emission excited by UV photons from O and B stars roughly correlates with other star-formation rate (SFR) indicators such as $\text{H}\alpha$ luminosity and $24\ \mu\text{m}$ continuum luminosity (Roussel et al. 2001). However, there is a large scatter, with PAH luminosity depending on metallicity and age of the stellar population (Calzetti et al. 2007). X-ray radiation from an AGN can destroy PAHs (Voit 1991), but should have little effect at large distances or in regions shielded from the nucleus. With these caveats in mind, we estimate the SFR from the luminosity of the $7.7\ \mu\text{m}$ PAH feature to be $7 \pm 3 \times 10^{-2}\ M_\odot\ \text{yr}^{-1}$ for 3C 326 N. The $24\ \mu\text{m}$ luminosity measured with MIPS yields a comparable SFR of $0.14 \pm 0.02\ M_\odot\ \text{yr}^{-1}$. The similarity of these two estimates indicates that the AGN does not dominate the continuum at this wavelength ($\lesssim 50\%$). The star formation rate is only 2 – 5% of the $\sim 3\ M_\odot\ \text{yr}^{-1}$ SFR of the Milky Way.

A remarkable aspect of 3C 326 N (and MOHEGs in general) is the lack of starburst activity in the presence of a large molecular gas mass. The mean surface density of warm H_2 inside the SL slit is $30\ M_\odot\ \text{pc}^{-2}$. In order to suppress star formation in a central thin disk, the total gas surface density must be below the critical density (Kennicutt 1989). An accurate estimate of the critical density in 3C 326 N will require a kinematic study of the molecular

gas. A large turbulent velocity dispersion or rotational velocity shear would increase the critical density for star formation. The molecular gas may have not yet even settled into a disk. Efficient star formation and AGN accretion may be suppressed and delayed in 3C 326 N until the molecular gas has kinematically settled and cooled.

The PAH and 24 μm luminosities of companion galaxy 3C 326 S yield estimated SFRs of $0.20 \pm 0.05 M_{\odot} \text{ yr}^{-1}$ and $0.26 \pm 0.03 M_{\odot} \text{ yr}^{-1}$, respectively. These SFR estimates are within the broad range seen for normal, non-starburst early type galaxies (Combes, Young, & Bureau 2007). The SFR in 3C 326 S is significantly larger than the SFR in 3C 326 N. Since no H_2 emission lines are detected, it is likely that most of the remaining molecular gas is cold and conducive to star formation. A *Hubble* Space Telescope image of 3C 326 S in the F702W band shows a dust lane (or nearly edge-on disk) cutting across the core at $\text{PA} \sim 105^\circ$, which confirms the presence of a significant dusty ISM (Martel et al. 1999). The galaxy 3C 326 S may be the H_2 donor for 3C 326 N, and may have had a much larger molecular gas component which has been largely stripped by tidal interaction. It would be particularly useful to measure the masses and surface densities of cold CO (and thereby H_2) in both galaxies to see if they are consistent with the observed SFRs and to help understand why the warm H_2 emission is so much stronger in 3C 326 N.

7. Energetics and H_2 Heating Mechanisms

In 3C 326 N, the ratio of mid-IR rotational H_2 emission to the 8-70 μm IR continuum emission is $L(\text{H}_2)/L_{8-70} = 0.17 \pm 0.02$. The H_2 pure rotational lines are therefore a major coolant for the warm molecular gas phase of the ISM. The 125 K H_2 component has a thermal energy content of $\sim 4 \times 10^{52}$ erg and the cooling time from the observed luminosity in H_2 S(0)+S(1) lines is only 9×10^3 yr. It is therefore necessary to continuously inject energy into the molecular gas to maintain the observed temperature. We consider below two possible scenarios for heating the H_2 , i) shock-heating by the inner radio jet and ii) tidally-induced inflow or accretion from the companion galaxy 3C 326 S.

7.1. Radio Jet Heating Scenario

The radio lobe size and Alfvén speed give an estimated expansion age of $\sim 2 \times 10^8$ yr for the Mpc-scale radio source (Willis & Strom 1978). The terminal working surfaces of the radio jets are in intergalactic space, far outside both galaxies. Any jet-heating of H_2 must be done locally by the inner jet at a radius of $\lesssim 3.1$ kpc. The average jet power is

best estimated from the extended radio lobe emission. The minimum energy content in the radio lobes derived from equipartition arguments is 6.0×10^{59} erg (Willis & Strom 1978). Dividing by the radio source lifetime, we estimate a jet kinetic luminosity of 9.5×10^{43} erg s^{-1} . We estimate a smaller kinetic luminosity of 4.8×10^{43} erg s^{-1} if the lobe magnetic fields have sub-equipartition strength and the lobe energy is dominated by relativistic particles (Punsly 2006, 2005).

The integrated 10 MHz-10 GHz synchrotron luminosity from the radio lobes is 4.7×10^{42} erg s^{-1} , $\sim 5\%$ of the estimated jet kinetic luminosity. The synchrotron luminosity of the 3C 326 N core is much weaker, at 3.5×10^{39} erg s^{-1} . If we assume that the synchrotron luminosity is roughly proportional to the dissipation of jet kinetic energy, then the ratio of core to lobe total luminosity indicates that $\sim 7 \times 10^{-4}$ of the jet kinetic luminosity, or $\sim 7 \times 10^{40}$ erg s^{-1} is dissipated in 3C 326 N. (For the sake of illustration, this assumes that relativistic beaming is not important in the core. In the likely case that the core emission is beamed, this should be divided by the beaming factor.) This is less than one tenth of the luminosity required to power the observed H_2 emission. Also, jet shocks must be active over a large fraction of the total H_2 mass in the galaxy to be a viable heating mechanism. However, with a large uncertainty in the amount of jet kinetic power dissipated and the unknown spatial configuration of H_2 , this scenario may deserve further consideration. High-spatial resolution radio observations are necessary to look for any direct evidence of jet-ISM interaction.

7.2. Tidally Induced Inflow

Another, preferred scenario is that 3C 326 N has been disturbed by gravitational interaction with 3C 326 S. The H_2 may have either been stripped from 3C 326 S, or already present in 3C 326 N. Tidal forces from 3C 326 S would then induce the observed distortions in 3C 326 N, in turn giving rise to gravitational torque that drives molecular gas into the galaxy center. The gravitational energy of the in-falling gas is then converted into turbulence and heat via an accretion shock or shocks between sub-clumps. The simulations of Mihos & Hernquist (1996) show that the greatest gas inflow rates are achieved for co-planar interactions of disk systems $\sim 2 \times 10^8$ yr after the initial encounter due to the growth of a central bar over the disk dynamical time scale, but before the final merger. The tidal field of the bar drives the inflow.

The K-band magnitudes of 3C 326 N and S are 12.95 and 13.60, respectively (Lilly & Longair 1984; Rawlings et al. 1990). We estimate stellar bulge masses of $3.1 \times 10^{11} M_\odot$ and $1.6 \times 10^{11} M_\odot$, respectively, using an empirical relation between K-band luminosity and bulge mass (Marconi & Hunt 2003). The $\sim 2:1$ mass ratio qualifies this as a major interaction. The

corresponding nuclear supermassive black hole masses (assuming $M_{\text{BH}}/M_{\text{bulge}} = 1.5 \times 10^{-3}$) are $\sim 5 \times 10^8 M_{\odot}$ and $\sim 2 \times 10^8 M_{\odot}$, which may eventually result in a major black hole merger if the two galaxies merge. The isophotes of 3C 326 N are roughly elliptical at a radius of $12''.2$, with $\text{PA} = 154^\circ$. At larger radii ($12 - 16''$), the isophotes bend to the south to meet 3C 326 S, perhaps indicating a tidal bridge. The two galaxies have identical radial velocities to within the measurement uncertainties ($\pm 300 \text{ km s}^{-1}$).

The 2-body L1 Lagrange point is at $24/\cos(\theta)$ kpc from the nucleus of 3C 326 N and $17/\cos(\theta)$ kpc from the nucleus of 3C 326 S, where θ is the inclination of the orbital axis. The gravitational potential energy released by $1.1 \times 10^9 M_{\odot}$ of H_2 falling from L1 to the center of 3C 326 N is 8.4×10^{57} erg. Dividing by the dynamical (free-fall) time-scale of $t_{\text{dyn}} = 9.1 \times 10^7$ yr, we obtain an H_2 inflow rate of $12 M_{\odot} \text{ yr}^{-1}$ and an accretion luminosity of 2.9×10^{42} erg s^{-1} . This is sufficient to power the observed H_2 emission at a conversion efficiency of 27%. A massive dark halo will deepen the gravitational potential and allow an even lower conversion efficiency. The near-coincidence of the crossing time-scale $2t_{\text{dyn}} = 1.8 \times 10^8$ yr and the age of the radio source suggests the intriguing possibility that the radio jet activity is ultimately fueled, at low radiative efficiency, by tidally driven accretion.

Ground-based adaptive-optics imaging of near-IR H_2 *rovibrational* transitions in 3C 326 N will probe the spatial distribution of hot H_2 and further test the scenario of tidally induced accretion. The proposed H_2 Explorer mission (H2EX, Boulanger & Maillard 2007), sensitive to H_2 emission over a large field of view, can establish the space density of the general MOHEG population and help determine its importance as a stage in galaxy evolution.

8. Conclusions

We have discovered extremely luminous molecular hydrogen pure-rotational emission lines from radio galaxy 3C 326 N. The continuum emission is relatively weak, so that the H_2 emission contributes 17% of the 8-70 μm IR luminosity and is a major coolant. We measure a warm molecular gas mass of $1.1 \times 10^9 M_{\odot}$ at temperatures of 125-1000 K within a 3.1 kpc radius of the galaxy center. The H_2 ortho/para ratios are consistent with thermodynamic equilibrium.

We consider 3 ways to heat the H_2 to the observed temperatures and produce the extreme H_2 emission line luminosities. The LINER AGN in 3C 326 N is most likely not luminous enough to power the observed H_2 emission via X-ray heating. Jet-shock heating could work in principle, but there does not appear to be enough kinetic energy dissipated inside the host galaxy by the jet. We favor the idea that accretion shocks from inflow induced

by tidal interaction with 3C 326 S may power the remarkable H_2 emission spectrum.

Weak PAH emission features and thermal dust continuum in 3C 326 N and 3C 326 S indicate very little star formation activity $\sim 0.1\text{--}0.3 M_\odot \text{ yr}^{-1}$. The weak star formation in 3C 326 N and low accretion luminosity of the AGN are remarkable considering the large amount and high surface density of molecular gas. Similar H_2 emission seen in some ULIRGs is usually accompanied by vigorous starburst or AGN activity. The newly discovered molecular hydrogen emission galaxy (MOHEG) phenomenon may represent an important stage in galaxy evolution. Star-formation as well as accretion onto the central supermassive black hole may be suppressed by high temperatures, turbulence, or velocity shear in the large central mass of shocked molecular gas.

This work is based on observations made with the *Spitzer* Space Telescope, which is operated by the Jet Propulsion Laboratory (JPL), California Institute of Technology (Caltech) under NASA contract. Support for this research was provided by NASA through an award issued by JPL/Caltech. This research has made use of the NASA/IPAC Extragalactic Database (NED) which is operated by JPL/Caltech, under contract with NASA. The IRAC 3-color image was processed using Montage, funded by NASA’s Earth Science Technology Office, Computation Technologies Project, and maintained by the NASA/IPAC Infrared Science Archive (IRSA). We made use of data from the Sloan Digital Sky Survey funded by the Alfred P. Sloan Foundation, Participating Institutions, NSF, NASA, U.S. DOE, Japanese Monbukagakusho, Max Planck Society, and the Higher Education Funding Council for England. Thanks to K. Sheth for enlightening discussions on star formation in galaxies. Thanks also to T. Jarrett and R.-R. Chary for help with IRAC.

REFERENCES

- Appleton, P. N. et al. 2006, ApJ, 639, L51
- Armus, L. et al. 2006, ApJ, 640, 204
- Boulanger, F. & Maillard, J. P. 2007, in CUP Conf. Series, Studying Galaxy Evolution with *Spitzer* and *Herschel*, ed. V. Charmandaris, D. Rigopoulou, & N. Kylafis, in press
- Calzetti, D. et al. 2007, ApJ, in press, arXiv:0705.3377
- Combes, F., Young, L. M., & Bureau, M. 2007, MNRAS, 377, 1795
- Donahue, M., Mack, J., Voit, G. M., Sparks, W., Elston, R., & Maloney, P. R. 2000, ApJ, 545, 670

- Draine, B. T. & Woods, D. T. 1990, *ApJ*, 363, 464
- Egami, E., Rieke, G. H., Fadda, D., & Hines, D. C. 2006, *ApJ*, 652, L21
- Fazio, G. G. et al. 2004, *ApJS*, 154, 10
- Haas, M., Chini, R., & Klaas, U. 2005, *A&A* 433, L17
- Hardcastle, M. J., Evans, D. A., & Croston, J. H. 2006, *MNRAS*, 370, 1893
- Hatch, N. A., Crawford, C. S., Johnstone, R. M., & Fabian A. C. 2005, *MNRAS*, 358, 765
- Higdon, S. J. U., Armus, L., Higdon, J. L., Soifer, B. T., & Spoon, H. W. W., 2006, *ApJ*, 648, 323
- Houck, J. R. et al. *ApJS*, 154, 18
- Johnstone, R. M., Hatch, N. A., Ferland, G. G., Fabian, A. C., Crawford, C.S., & Wilman, R. J. 2007, in press ([astro-ph/0702431](#))
- Kennicutt, R. 1989, *ApJ*, 344, 685
- Klaas, U., Haas, M., Heinrichsen, I., & Schulz, B. 1997, *A&A*, 325, L21
- Krolik, J. H. & Lepp, S. 1989, *ApJ*, 347, 179
- Le Bourlot, J., Pineau des Forets, G., & Flower, D. R. 1999, *MNRAS*, 305, 802
- Lilly, S. & Longair, M. S. 1984, *MNRAS*, 211, 833
- Lutz, D., Sturm, E., Genzel, R., Spoon, H. W. W., Moorwood, A. F. M., Netzer, H., & Sternberg A. 2003, *A&A*, 409, 867
- Marconi, A., & Hunt, L. K. 2003, *ApJ*, 589, L21
- Martel, A. et al. 1999, *ApJS*, 122, 81
- Max, C., Canalizo, G., Macintosh, B. A., Raschke, L., Whysong, D., Antonucci, R., & Schneider, G. 2005, *ApJ*, 621, 738
- Mihos, C., & Hernquist, L. 1996, *ApJ*, 464, 641
- Netzer, H., Lemze, D., Kaspi, S., George, I. M., Turner, T. J., Lutz, D., Boller, T., & Chelouche, D. 2005, *ApJ*, 629, 739
- Neufeld, D. A. et al. 2006, *ApJ*, 649, 816

- Ogle, P., Whysong, D., & Antonucci, R. 2006, *ApJ*, 647, 161
- Ogle, P. M., Antonucci, R., & Whysong, D. W. 2007, in *ASP Conf. Ser.*, The Central Engine of Active Galactic Nuclei, ed. L. C. Ho & J.-M. Wang, in press, (astro-ph/0612443)
- Punsly, B., 2005, *ApJ*, 623, L9
- Punsly, B., 2006, *ApJ*, 651, 17
- Quillen, A. C., Almog, J., & Yukita, M. 2003, *AJ*, 126, 2677
- Rawlings, S., Saunders, R., Miller, P., & Jones, M. E. 1990, *MNRAS*, 246, 21P
- Reynolds, C. S., Di Matteo, T., Fabian, A. C., Hwang, U., & Canizares, C. R. 1996, *MNRAS*, 283, 111
- Rieke, G. H. et al. 2004, *ApJS*, 154, 25
- Rigopoulou, D., Kunze, D., Lutz, D., Genzel, R., & Moorwood, A. F. M. 2002, *A&A*, 389, 374
- Roussel, H., 2007, *ApJS*, in press, arXiv:0707.0395
- Roussel, H., Sauvage, M., Vigroux, L., and Bosma, A. 2001, *A&A*, 372, 427
- Shi, Y. et al. 2007, *ApJ*, submitted
- Simpson, C., Ward, M., Clements, D. L., & Rawlings, S. 1996, *MNRAS*, 281, 509
- Smith, J. D., et al. 2007, *ApJ*, 656, 770
- Spinoglio, L. & Malkan, M. 1992, *ApJ*, 399, 504
- Sturm, E. et al. 2006, *ApJ*, 653, L13
- Voit, M. 1991, *ApJ*, 379, 122
- Willis, A. G. & Strom, R. G. 1978, *A&A*, 62, 375
- Wilgenbus, D., Cabrit, S., Pineau des Forets, G., & Flower, D. R. 2000, *A&A* 356, 1010
- Xu, C. K., Lu, N., Condon, J.J., Dopita, M., & Tuffs, R. J. 2003, *ApJ*, 595, 665
- Young, J., Xie, S., Tacconi, L. et al. 1995, *ApJS*, 98, 219

Table 1. H₂ 0-0 S(J) Emission Lines

| | H ₂ S(0) | S(1) | S(2) | S(3) | S(4) | S(5) | S(6) | S(7) |
|------------------------------|---------------------|------------|------------|------------|------------|------------|--------------|--------------|
| $\lambda(\mu\text{m, rest})$ | 28.22 | 17.04 | 12.28 | 9.66 | 8.03 | 6.91 | 6.11 | 5.51 |
| Flux ^a | 0.24(0.03) | 0.58(0.05) | 0.39(0.04) | 1.18(0.04) | 0.28(0.06) | 0.86(0.15) | 0.24(0.08) | 0.28(0.08) |
| EW ^b | 1.9(0.6) | 1.3(0.2) | 0.41(0.08) | 0.80(0.08) | 0.14(0.03) | 0.34(0.10) | 0.074(0.025) | 0.066(0.022) |
| Luminosity ^c | 0.48 | 1.1 | 0.77 | 2.34 | 0.55 | 1.7 | 0.48 | 0.55 |
| N/g^d | 9.2E18 | 2.8E17 | 3.8E16 | 6.9E15 | 1.3E15 | 4.4E14 | 1.5E14 | 2.7E13 |

^aFlux (10^{-14} erg s⁻¹ cm⁻²).

^bEquivalent Width ($\mu\text{m, rest}$).

^c Luminosity (10^{41} erg s⁻¹), at a luminosity distance of 407 Mpc.

^dColumn Density (cm⁻²) of upper level divided by its statistical weight, assuming a $3''.7 \times 3''.7$ source.

Table 2. Forbidden Emission Lines

| | [Fe II] | [S IV] | [Ne II] | [S III] | [O IV] |
|------------------------------|------------|------------|------------|------------|------------|
| $\lambda(\mu\text{m, rest})$ | 5.34 | 10.51 | 12.81 | 18.71 | 25.89 |
| Flux ^a | 0.20(0.08) | 0.08(0.04) | 0.40(0.04) | 0.14(0.07) | 0.25(0.03) |
| Flux/[Ne II] | 0.5(0.2) | 0.2(0.1) | 1.0 | 0.4(0.2) | 0.6(0.1) |

^aFlux (10^{-14} erg s⁻¹ cm⁻²).

Table 3. Aromatic Emission Features (PAHs)

| $\lambda(\mu\text{m})$ | 6.7 | 7.7 | 10.7 | 11.3 | 13.6 | 15.9 | 17 | 18.9 |
|------------------------|------------|------------|-----------|------------|------------|------------|------------|------------|
| 3C 326 N | 1.13(0.48) | 0.53(0.26) | 0.22(.09) | 0.64(0.13) | 0.98(0.18) | 0.21(0.11) | 1.15(0.27) | 0.33(0.18) |
| 3C 326 S | ... | 1.61(0.42) | ... | 1.19(0.20) | ... | ... | ... | ... |

^aFlux (10^{-14} erg s $^{-1}$ cm $^{-2}$).

Table 4. MIPS 24, 70, and 160 μm Photometry

| | $F_\nu(24 \mu\text{m})^{\text{a}}$ | $F_\nu(70 \mu\text{m})^{\text{b}}$ | $F_\nu(160 \mu\text{m})^{\text{c}}$ | $L(24 \mu\text{m})^{\text{d}}$ | $L(70 \mu\text{m})$ | $L(70)/L(24)$ |
|---------------------|------------------------------------|------------------------------------|-------------------------------------|--------------------------------|---------------------|---------------|
| 3C 326 N | 0.52 ± 0.07 | 6.12 ± 0.65 | < 34 | 1.3 ± 0.2 | 5.2 ± 0.6 | 4.0 ± 0.8 |
| 3C 326 S | 1.05 ± 0.12 | 4.33 ± 0.60 | < 34 | 2.6 ± 0.3 | 3.7 ± 0.5 | 1.4 ± 0.3 |
| bridge ^e | ... | 4.40 ± 0.60 | ... | ... | 3.8 ± 0.5 | ... |

^aFlux density (mJy) in the 24 μm band, measured in a $4''.9$ radius aperture and multiplied by an aperture correction of 2.0.

^bFlux density (mJy) in the 70 μm band, measured in a $9''.84$ radius aperture and multiplied by an aperture correction of 1.5.

^cThe 3σ upper limit to the 160 μm flux density (mJy), measured in a $20''$ radius aperture.

^d Luminosity $\nu L_\nu (10^{42} \text{ erg s}^{-1})$, at a luminosity distance of 407 Mpc.

^eThis source (only in the MIPS 70 μm image) is found at roughly the location where the tidal bridge appears to connect to 3C 326 N (Fig. 5).

Table 5. H₂ Model Parameters

| T(K) | $M(\text{H}_2)^{\text{a}}$ | Ortho/Para | $n_{\text{crit}}^{\text{b}}$ | $f_{\text{max}}^{\text{c}}$ |
|------|----------------------------|------------|------------------------------|-----------------------------|
| 125 | 1.1E9 | 2.1 | 5.3E2 | 1.5E-3 |
| 400 | 1.1E7 | 3.0 | 1.1E4 | 7.0E-7 |
| 1000 | 6.4E5 | 3.0 | 4.4E5 | 1.0E-9 |

^aH₂ mass (M_{\odot}).

^bCritical density (cm^{-3}).

^cMaximum filling factor under LTE conditions.

Table 6. Strong H₂ Emitters

| | M(cold H ₂) ^a | M(warm H ₂) ^b | $L(H_2)^c$ | $L(H_2)/L(IR)^d$ | Refs. |
|-------------------|--------------------------------------|--------------------------------------|------------------------|------------------|-------|
| Zw 3146 BCG | $\sim 1 \times 10^{11}$ | $\sim 1 \times 10^{10}$ | 2.1×10^{43} | 0.014 | 1 |
| NGC 6240 | 1.1×10^{10} | 1.6×10^9 | 4.6×10^{42} | 0.003 | 2,3 |
| 3C 326 N | ... | 1.1×10^9 | 8.0×10^{41} | 0.04-0.1 | |
| Antennae | 9.6×10^9 | 4.9×10^8 | 1.7×10^{41} | 0.0009 | 4,5,6 |
| Stephan's Quintet | ... | $> 3.4 \times 10^7$ | $> 8.4 \times 10^{40}$ | 0.34 | 7 |

^aCold H₂ mass derived from CO measurements.

^bWarm H₂ mass measured from Spitzer or ISO spectra.

^cH₂ Luminosity (erg s⁻¹).

^dThe IR luminosity is integrated over 8-1000 μ m.

References. — (1) Egami et al. 2006; (2) Lutz et al. 2003; (3) Armus et al. 2006; (4) Haas et al. 2005; (5) Young et al. 1995; (6) Klaas et al. 1997; (7) Appleton et al. 2006.

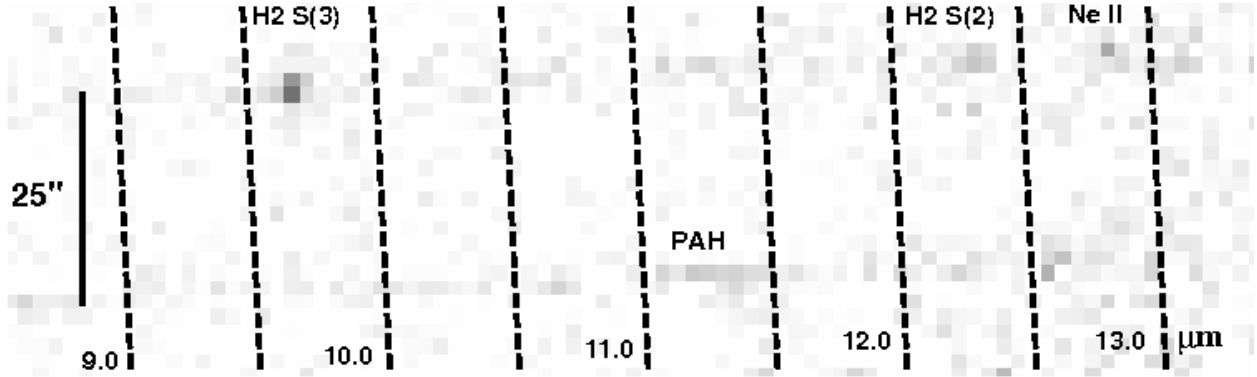


Fig. 1.— *Spitzer* IRS SL1 8.5-13.4 μm (rest) 2D spectra of 3C 326 N (*top*) and 3C 326 S (*bottom*). The bright H_2 S(3) 9.66 μm emission line in 3C 326 N is spatially and spectrally unresolved. The H_2 S(2) and Ne II lines are also seen. The southern galaxy was serendipitously placed precisely on the SL slit (PA= 178°). Its 11.3 μm PAH emission feature is indicated.

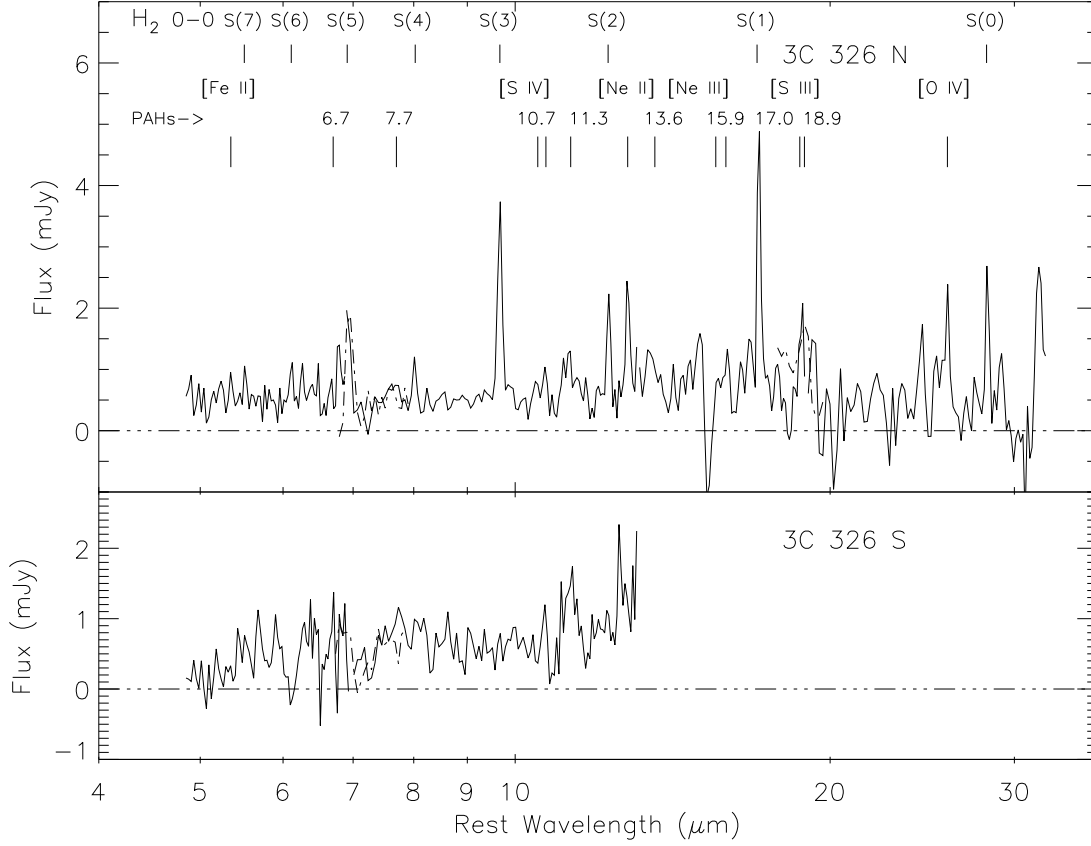


Fig. 2.— *Top*: *Spitzer* IRS spectrum of 3C 326 N. *Dashed lines*—SL3 and LL3 bonus orders. Extremely strong H₂ emission lines of high equivalent width dominate the spectrum. Weak PAH features indicate a very low level of star formation in spite of the large amount of H₂. Forbidden ionic emission line ratios are consistent with a weak LINER AGN. *Bottom*: PAH emission is detected in 3C 326 S, but no H₂ or ionic forbidden lines.

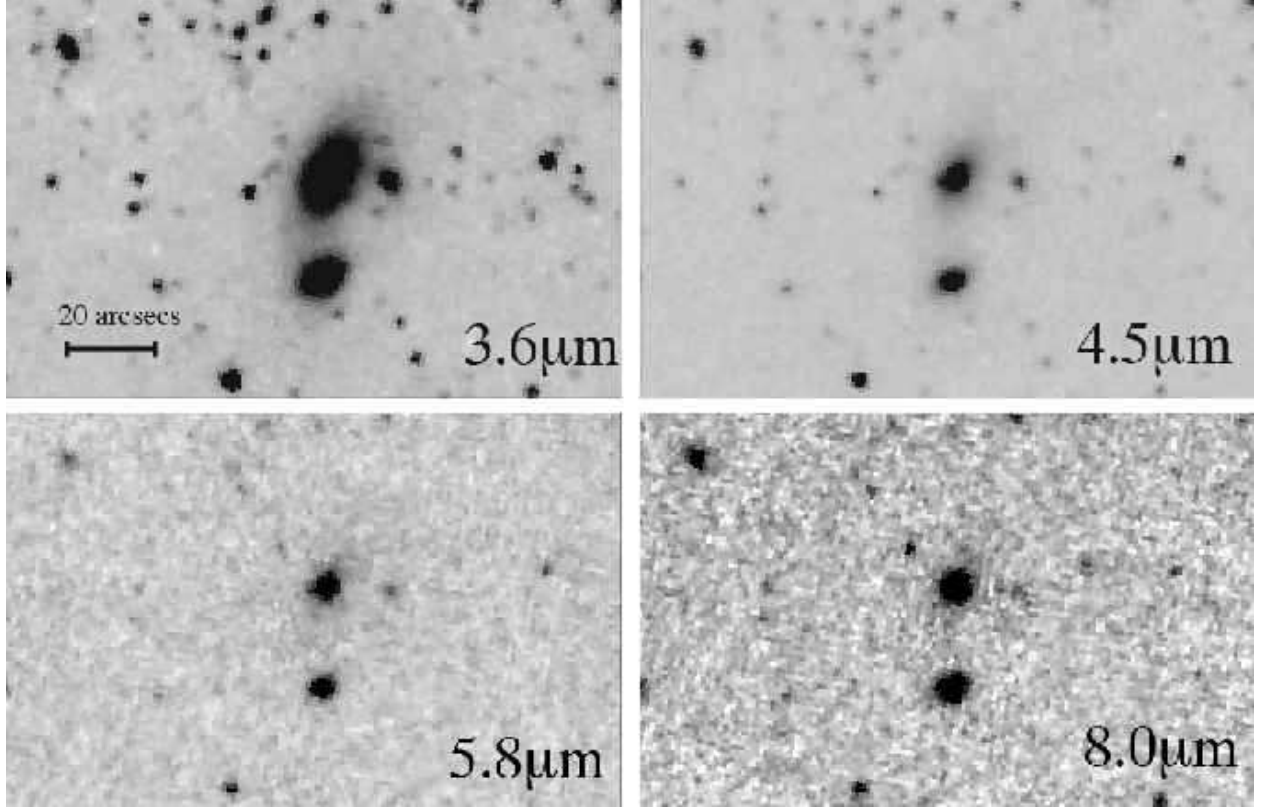


Fig. 3.— *Spitzer* IRAC 3.6, 4.5, 5.8, and 8.0 μm images of 3C 326. North is at top, East to the left. The first two bands are dominated by stellar emission, while the second two have contributions from dust and H_2 . The galaxies 3C 326 N and 3C 326 S are the brightest two sources in these images. A third source at $\text{PA} = 268^\circ$ and a fourth $4''.3$ away from 3C 326 N at $\text{PA} = 111^\circ$ (seen protruding from the left of the galaxy core in the 4.5 μm image) appear to be unrelated galaxies seen in projection (see §3.3). Note the apparent tidal bridge between 3C 326 N and S and a possible tidal tail to the NW in the 3.6 and 4.5 μm images, evidence of an ongoing galaxy collision. The galaxy cores are barely resolved at 5.8 μm , and 3C 326 S is nearly as bright as 3C 326 N at 8.0 μm .



Fig. 4.— *Spitzer* IRAC 3-color image of 3C 326. Blue = $3.6\ \mu\text{m}$, green= $4.5\ \mu\text{m}$, red= $5.8\ \mu\text{m}$. Foreground stars and starlight-dominated galaxies appear blue-green, while dust or H_2 emission appears red. The brightest galaxy and AGN host 3C 326 N has an irregular morphology because of its interaction with 3C 326 S. Note the possible tidal tail extending to the NW.

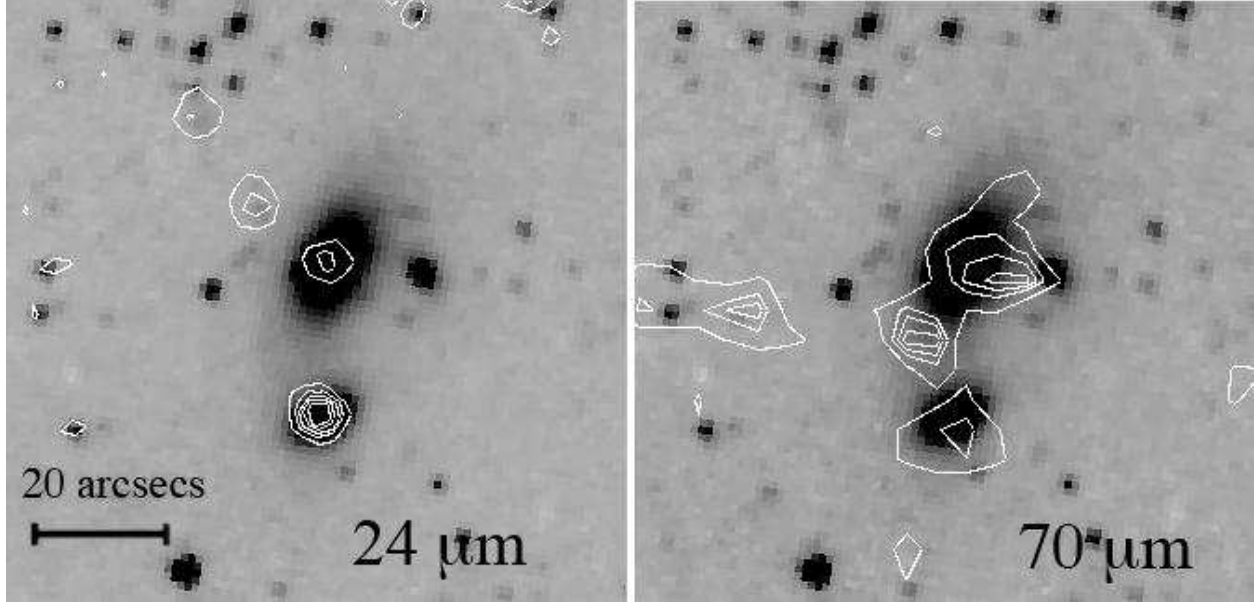


Fig. 5.— *Left:* *Spitzer* MIPS 24 μm flux contours overlaid on the IRAC 3.6 μm image of 3C 326. North is at top, East to the left. The contour levels are 0.3, 0.4, 0.5, and 0.6 MJy/sr. *Right:* MIPS 70 μm contours overlaid on the 3.6 μm image. The contour levels are 0.45, 0.65, 0.75 and 0.85 MJy/sr. 3C 326 S is brighter at 24 μm , while 3C 326 N is brighter at 70 μm . A third 70 μm source appears between the two galaxies, but not in the IRAC image. It may be cool dust emission associated with the tidal bridge, or an unrelated background source.

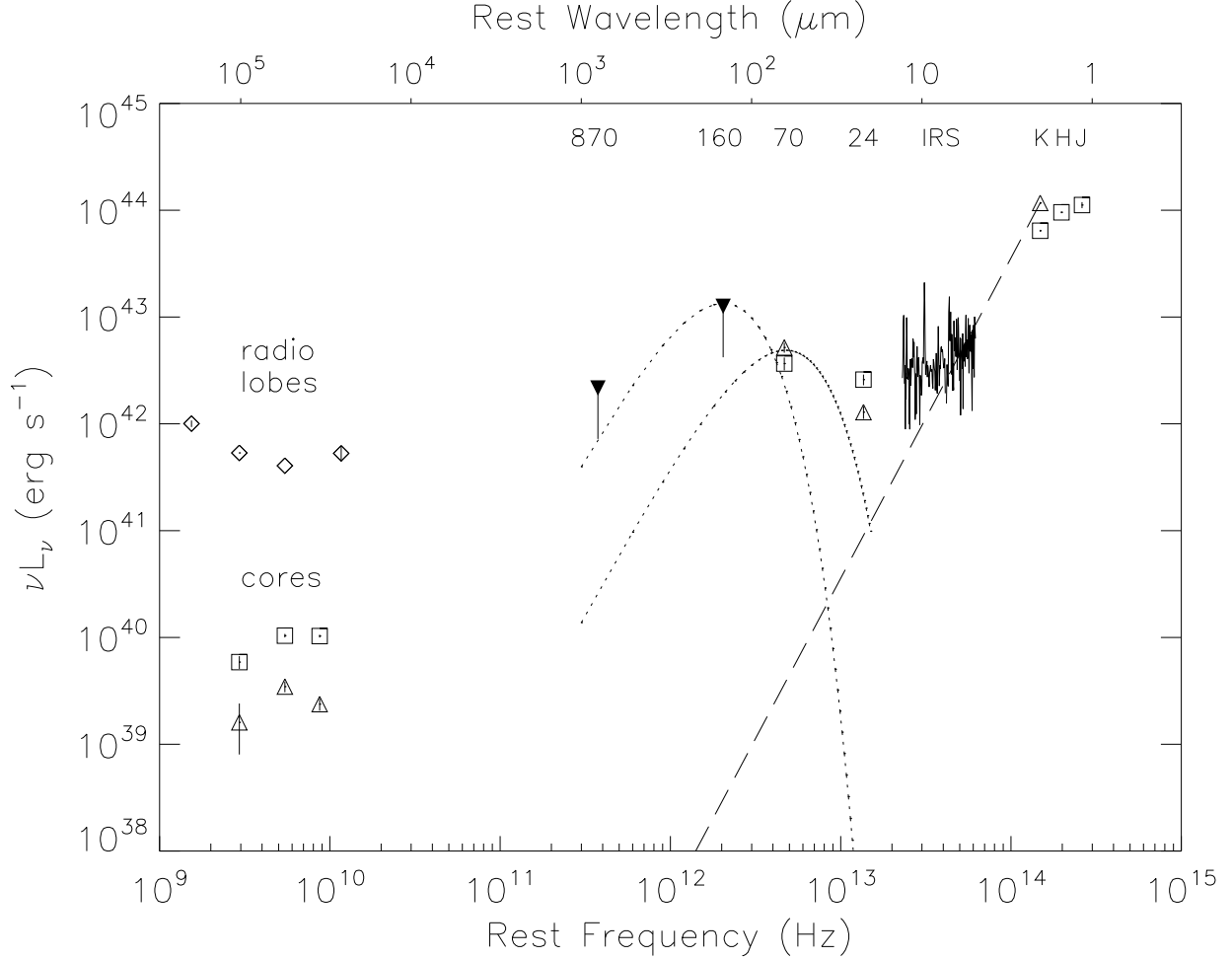


Fig. 6.— Spectral energy distributions of 3C 326 N (*open triangles and solid line*), 3C 326 S (*squares*), and 3C 326 radio lobes (*diamonds*). MIPS 24 and 70 μm points indicate warm and cold dust components. MIPS 160 μm and ground-based 870 μm (Quillen et al. 2003) 3σ upper limits (*inverted triangles*) apply to both galaxies individually. J, H, and K-band near-IR photometry are by Lilly & Longair (1984). The radio core fluxes and the K-band photometry of 3C 326 N are from Rawlings et al. (1990). Radio lobe data are from Willis & Strom (1978) and the NASA/IPAC Extragalactic Database (NED). The dashed line represents the Rayleigh-Jeans tail of starlight connecting the K-band photometry to the IRS spectrum of 3C 326 N. The dotted lines are 25 and 58 K blackbodies, representing upper and lower limits to the 70-1000 μm emission.

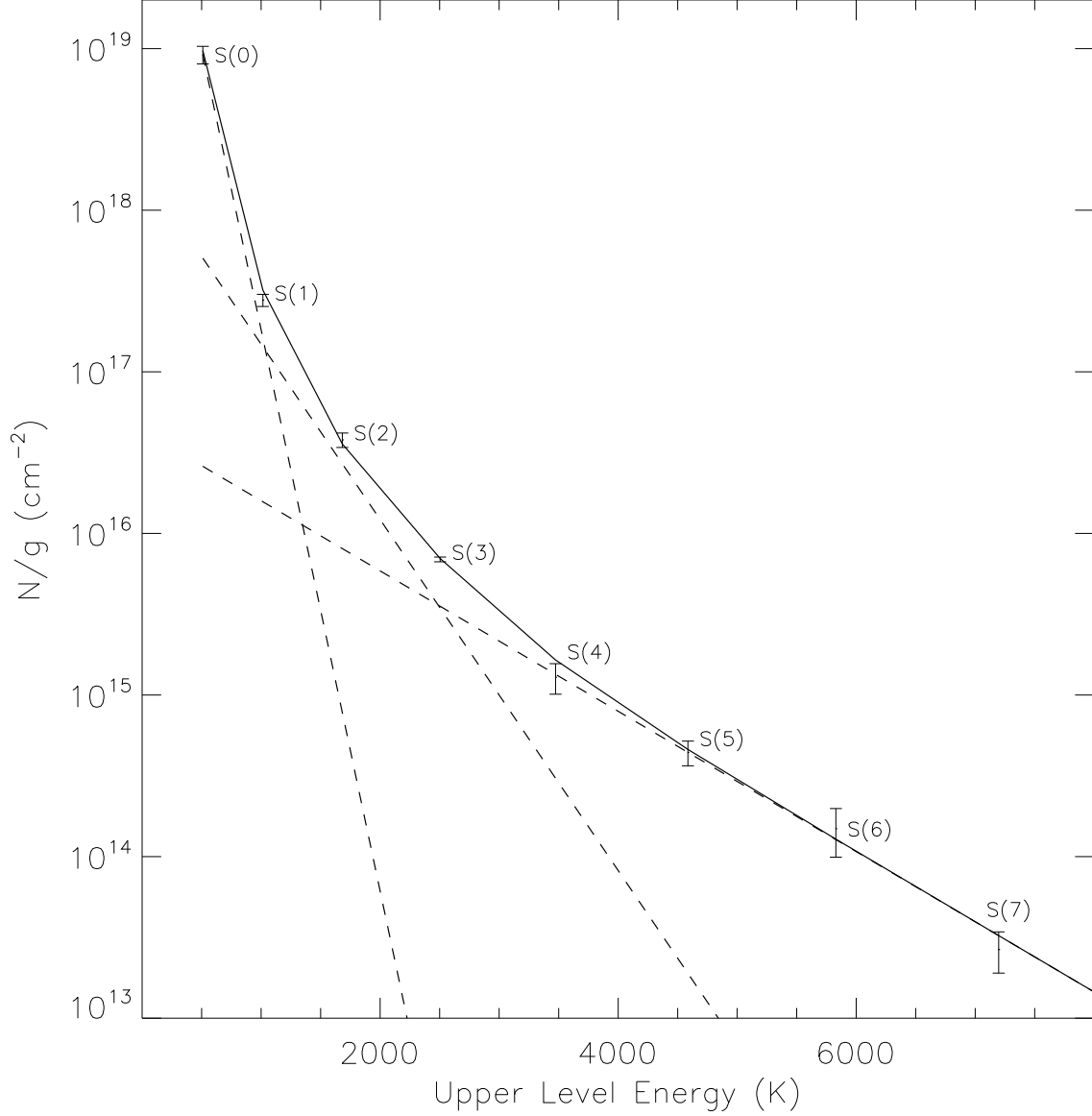


Fig. 7.— H_2 excitation diagram for 3C 326 N. Upper-level column densities normalized by their statistical weights are plotted as a function of upper-level energy (E_u/k_B) for each pure-rotational transition. The best-fitting model (*solid line*) has 3 temperature components (*dashed lines*): 125, 400, and 1000 K. The ortho/para ratios are set at the respective thermal equilibrium values (Table 5). Note that the y-intercept for each model component gives the average H_2 ground-state column density integrated over the SL slit.